The Astrophysical Journal, 984:79 (13pp), 2025 May 1 https://doi.org/10.3847/1538-4357/adc4e8

Chandra Discovery of a Candidate Hyperluminous X-Ray Source in MCG+11-11-032

Adi Foord[1], Francesca Civano[2], Julia M. Comerford[3], Martin Elvis[4], Giuseppina Fabbiano[4], Tingting Liu[5], Elisabeta Lusso[6,7], Stefano Marchesi[8,9,10], Mar Mezcua[11,12], Francisco Muller-Sanchez[13], Rebecca Nevin[14], and Kristina Nyland[15]

[1] Department of Physics, University of Maryland Baltimore County, 1000 Hilltop Cir, Baltimore, MD 21250, USA
[2] NASA Goddard Space Flight Center, Greenbelt, MD 20771, USA
[3] Department of Astrophysical and Planetary Sciences, University of Colorado, Boulder, CO 80309, USA
[4] Harvard-Smithsonian Center for Astrophysics, 60 Garden St., Cambridge, MA 02138, USA
[5] Department of Physics and Astronomy, West Virginia University, P.O. Box 6315, Morgantown, WV 26506, USA
[6] Dipartamento di Fisica e Astronomia, Universitá di Firenze, Via G. Sansone 1, 50019 Sesto Fiorentino, FI, Italy
[7] INAF—Osservatorio Astrofisico di Arcetri, Largo E.Fermi 5, 50125 Firenze, Italy
[8] Dipartimento di Fisica e Astronomia (DIFA), Universitá di Bologna, via Gobetti 93/2, I-40129 Bologna, Italy
[9] Department of Physics and Astronomy, Clemson University, Kinard Lab of Physics, Clemson, SC 29634-0978, USA
[10] INAF—Osservatorio di Astrofisica e Scienza dello Spazio di Bologna, Via Piero Gobetti, 93/3, 40129, Bologna, Italy
[11] Institute of Space Sciences (ICE, CSIC), Campus UAB, Carrer de Magrans, 08193 Barcelona, Spain
[12] Institut d'Estudis Espacials de Catalunya (IEEC), Edifici RDIT, Campus UPC, 08860 Castelldefels (Barcelona), Spain
[13] Department of Physics and Materials Science, The University of Memphis, 3720 Alumni Avenue, Memphis, TN 38152, USA
[14] Fermi National Accelerator Laboratory, P.O. Box 500, Batavia, IL 60510, USA
[15] U.S. Naval Research Laboratory, 4555 Overlook Ave. SW, Washington, DC 20375, USA

Received 2024 September 3; revised 2025 February 15; accepted 2025 March 13; published 2025 April 29

Abstract

We present a multiwavelength analysis of MCG+11-11-032, a nearby active galactic nucleus (AGN), with a unique classification as being both a binary and a dual AGN candidate. With new Chandra observations, we aim to resolve any dual AGN system via imaging data and search for signs of a binary AGN via analysis of the X-ray spectrum. Analyzing the Chandra spectrum, we find no evidence of the previously suggested double-peaked Fe Kα lines; the spectrum is instead best fit by an absorbed power law with a single Fe Kα line, as well as an additional line centered at ≈7.5 keV. The Chandra observation reveals faint, soft, and extended X-ray emission, possibly linked to low-level nuclear outflows. Further analysis shows evidence for a compact hard source—MCG+11-11-032 X2—located 3.″3 from the primary AGN. Modeling MCG+11-11-032 X2 as a compact source, we find that it is relatively luminous ($L_{2-10\,\mathrm{keV}} = 1.5^{+0.9}_{-0.5} \times 10^{41}\,\mathrm{erg\,s^{-1}}$), and the location is coincident with a compact and off-nuclear source resolved in Hubble Space Telescope infrared (F105W) and optical (F621M, F547M) bands. Pairing our X-ray results with a 144 MHz radio detection at the host galaxy location, we observe X-ray and radio properties similar to those of ESO 243-49 HLX-1, suggesting that MCG+11-11-032 X2 may be a hyperluminous X-ray source. This detection with Chandra highlights the importance of a high-resolution X-ray imager as well as how previous binary AGN candidates detected with large-aperture instruments can benefit from high-resolution follow-up. Future spatially resolved optical spectra, and deeper X-ray observations, can better constrain the origin of MCG+11-11-032 X2.

Unified Astronomy Thesaurus concepts: X-ray active galactic nuclei (2035); Galaxy mergers (608); Supermassive black holes (1663); Intermediate-mass black holes (816)

1. Introduction

MCG+11-11-032 is a nearby ($z = 0.0362$) Seyfert 2 galaxy, where the central active galactic nucleus (AGN) has the unique classification as being both a "dual AGN" candidate (J. M. Comerford et al. 2012) and a "binary AGN" candidate (P. Severgnini et al. 2018). Dual and binary AGNs are a natural consequence of galaxy–galaxy mergers (e.g., P. F. Hopkins et al. 2008; M. Volonteri et al. 2008; M. Colpi & M. Dotti 2011). During the stages of a galaxy merger where both central supermassive black holes (SMBHs) are brightly accreting as AGNs, the system can be classified as a dual AGN during the earliest stages (at kiloparsec-scale separations) and as a binary AGN at the final stages (where it has evolved down to subparsec separations; M. C. Begelman 2002).

The dual AGN classification stems from the double-peaked [O III] emission lines discovered in the Sloan Digital Sky Survey (SDSS) spectrum, with shifts in central wavelength that are inconsistent with the host galaxy redshift (J.-M. Wang et al. 2009). The source was then analyzed in J. M. Comerford et al. (2012), using the Blue Channel Spectrograph on the MMT 6.5 m telescope. J. M. Comerford et al. (2012) reported a velocity separation between the two [O III] peaks of 275 km s^{-1} and a projected separation on the sky of 0.″77 (corresponding to 0.55 kpc at $z = 0.0362$). The two line peaks were reported to be maximally separated at a position angle close to that of the galaxy's plane ($\mathrm{PA_{opt}} = 61°$). P. Severgnini et al. (2018) performed a second analysis of the SDSS spectrum of MCG +11-11-032, confirming the results found by J. M. Comerford et al. (2012) and reaching similar conclusions for the Hα, [N II], and [S II] emission-line velocity offsets. These results suggest the possibility of two distinct narrowline regions associated with a dual AGN, although other possibilities include a single AGN with outflows, disk rotation, and/or dust obscuration (e.g., R. Nevin et al. 2016).

P. Severgnini et al. (2018) analyzed the available Swift X-Ray Telescope (XRT) and Burst Alert Telescope (BAT) observations to further investigate the source. A variability analysis using Swift XRT (54 days of observations over a period of approximately 1 yr) showed the source varying between a bright and faint state (XRT count rates: bright—0.03 cts s^{-1}; faint—0.01 cts s^{-1}). Because the spectral properties remained consistent between the two states, P. Severgnini et al. (2018) concluded that the observed variability may be due to intrinsic flux variations, versus variable levels of absorption along the line of sight. The best-fit model to the XRT X-ray spectrum hinted at the presence of two emission lines at ∼6.16 keV (3σ) and ∼6.56 keV ($<2\sigma$), respectively. An analysis of the 123 month 15–150 keV BAT light curve showed evidence for a sinusoidal signal, with a period of approximately 25 months.

The velocity separation of the two emission lines (0.4 keV or $\sim 0.06c$) is inconsistent with the projected separation measured from the double-peaked optical narrow emission lines. P. Severgnini et al. (2018) proposed an alternative interpretation for this source, where the ∼25 month periodicity of the X-ray emission may be due to a subparsec binary SMBH system. Many numerical simulations have been performed to understand the nature of binary SMBH variability, finding that subparsec binary SMBHs can form a circumbinary disk (e.g., A. I. MacFadyen & M. Milosavljević 2008; D. J. D'Orazio et al. 2013, 2016; B. D. Farris et al. 2015; Y. Tang et al. 2018; M. S. L. Moody et al. 2019; P. C. Duffell et al. 2020; C. Tiede et al. 2020; A. Derdzinski et al. 2021; D. J. D'Orazio & P. C. Duffell 2021; K. Whitley et al. 2024). The mass accretion rate of this disk is modulated by the orbital period of the SMBH binary, resulting in the observed periodic X-ray emission (e.g., D. J. D'Orazio et al. 2013; B. D. Farris et al. 2014; R. Gold et al. 2014). Assuming a 25 month period and a mass of $5 \times 10^8 M_\odot$ (as measured from the velocity dispersion of the CO emission line; I. Lamperti et al. 2017), P. Severgnini et al. (2018) calculated an orbital velocity of $\sim 0.06c$, consistent with the velocity difference measured using the Fe Kα emission-line profiles in the X-ray spectrum. T. Liu et al. (2020) presented an analysis using publicly available BAT light-curve data of MCG +11-11-032 from the Third Palermo BAT Catalog (3PBC). They found that a sinusoidal signal is rejected at >90% confidence intervals; however, given that 3PBC only includes the first 66 months of the survey, robustly detecting two cycles of the signal is more difficult.

MCG+11-11-032 is thus a peculiar source, showing evidence for double-peaked emission lines in optical and (tentatively) X-ray spectra. Confirmation of either a dual or binary AGN nature can be achieved with the Chandra X-ray Observatory. If the observed narrow emission lines presented in J. M. Comerford et al. (2012) are possibly produced by two AGNs separated by $0\farcs77$, then Chandra can resolve them as two distinct X-ray sources. Alternatively, follow-up Chandra observations of the spectrum of MCG+11-11-032 allow for the confirmation of two narrow Fe emission lines near ∼6.4 keV, as presented in P. Severgnini et al. (2018). The subarcsecond spatial resolution and energy resolution of Chandra are necessary to better constrain the X-ray properties of MCG +11-11-032 and allow for further unexpected discoveries.

The remainder of the paper is organized into three sections. In Section 2, we analyze the new Chandra observation and search for evidence of either a dual AGN (via a spatial analysis) and/or a binary AGN (via a spectral analysis); in Section 3, we incorporate archival multiwavelength coverage into our analysis, to investigate sources resolved in the Chandra data set; and in Section 4, we summarize our findings. Throughout the paper, we assume a ΛCDM Universe, where $H_0 = 69.6\,\mathrm{km\,s^{-1}}$, $\Omega_M = 0.286$, and $\Omega_\Lambda = 0.714$.

2. X-Ray Analysis and Results

MCG+11-11-032 was targeted by Chandra in a Cycle 23 proposal (PI: Civano; ID: 23700236). The AGN was observed for 35 ks on 2023 July 3 (observation ID: 25367). The source was observed on-axis and placed on the back-illuminated S3 chip of the ACIS detector. The exposure time was set to achieve at least 1300 (3300) counts in the 0.5–8 keV band in the faint (bright) state, with the goal of constraining both of the putative Fe lines at $>3\sigma$. To avoid pileup, which could compromise the goal of separating two nuclei if the source should be in the bright state, MCG+11-11-032 was observed in a subarray mode (with a 1/8 chip subarray, reducing the nominal CCD integration time to 0.4 s).

We follow the standard data reduction for point-source observations, using the Chandra Interactive Analysis of Observations (`CIAO`) software, v4.12 (A. Fruscione et al. 2006). The first step is to correct for astrometry, crossmatching the Chandra-detected point-like sources with the SDSS Data Release 18 (DR18) catalog. The Chandra sources used for crossmatching are detected by running `wavdetect` on the reprocessed level 2 event file. We require the observation to have a minimum of three matches with SDSS DR18 and each matched pair to be less than $2''$ from one another. Because the observation for MCG+11-11-032 was taken in a subarray, we find that there are not enough X-ray point sources to match with the SDSS DR18 catalog. However, we note that all Chandra observations undergo aspect corrections via the AGASC catalog,[16] with current radial astrometric errors for on-axis sources of $\approx 0\farcs79$.[17] The lack of additional astrometric corrections has no effect on our X-ray data analysis: if it is a dual AGN, the locations of each putative AGN will be measured relative to the primary X-ray point source; and if it is a binary AGN, relative astrometric shifts will not affect our X-ray spectral analysis. Last, we find the background flaring contribution to be negligible, with no time interval containing a background rate 3σ above the mean level.

To quantitatively determine the presence of one or multiple point sources, we analyze the Chandra data with `BAYMAX` (see, e.g., A. Foord et al. 2019, 2020; B. Sandoval et al. 2024). `BAYMAX`: (1) takes calibrated Chandra events and compares them to the expected distribution of counts for single versus dual-point-source models; (2) calculates a Bayes factor to determine which model is preferred ($\log \mathcal{BF}$); (3) calculates likely values for the angular separation (r) and count ratio (f, the ratio between the secondary and primary source); (4) probabilistically assigns source counts to each model component; and (5) fits spectra to each component, allowing for estimates of the flux. In addition to each point-source component, all models include a background component, which is energy-independent and assumed to be uniformly distributed. For bright sources, the source counts and fluxes obtained by `BAYMAX` match the expected output using the

[16] https://cxc.harvard.edu/cgi-gen/cda/agasc/agascInterface.pl
[17] https://cxc.harvard.edu/cal/ASPECT/celmon/

standard CIAO tools (A. Foord et al. 2019, 2020). However, for low-count and/or closely separated components, the statistical spectral analysis carried out by BAYMAX allows for a more robust measure of X-ray properties.

For each source, the nested sampling technique that calculates the Bayes factors returns a statistical error bar. In past analyses, we have found that the statistical error bars are consistent with the 1σ spread in the $\log \mathcal{BF}$ values when running BAYMAX 100 times on a given observation (A. Foord et al. 2019, 2020, 2021). In the following section, we quote a 3σ error on the $\log \mathcal{BF}$ value using the statistical errors returned by BAYMAX. For data sets in a similar region of parameter space as our Chandra observation (on-axis observations with over 700 counts between 0.5 and 8 keV), we have previously quantified a "strong" Bayes factor by running BAYMAX on simulations of single AGNs and calculating the false-positive rate below various thresholds; all simulations were found to have $\log \mathrm{BF} < 0.54$ in favor of the dual point source, and thus we use this threshold to define a strong logBF value in favor of the dual-point-source model (A. Foord et al. 2019). With over 700 counts, we can expect to be sensitive to detecting dual AGNs down to angular separations of $0\farcs5$ at count ratio values $f \geqslant 0.1$. For detailed information on the statistics behind the code, we refer the reader to A. Foord et al. (2019).

2.1. Dual AGN Hypothesis: Spatial Analysis of Chandra Data Set

By eye, the Chandra observation shows additional X-ray emission approximately $3''$ away from the location of MCG +11-11-032. In Figure 1, we show the 0.5–8 keV Chandra observation. This separation is larger than the known placement of the artifact in Chandra's point-spread function and has a different position angle with respect to the feature's expected location (see Figure 1). We analyze the 0.5–8 keV counts with BAYMAX, using a $20'' \times 20''$ sky region centered on the nominal X-ray coordinates of the AGN (corresponding to a 13 kpc × 13 kpc box at $z = 0.0362$). Similar to previous analyses using BAYMAX (A. Foord et al. 2020, 2021; B. Sandoval et al. 2024), the single-point-source model's prior distributions include the source's sky coordinate, μ, and the logarithm of the background fraction, $\log f_{\mathrm{bkg}}$. The dual-point-source model's prior distributions include the sky coordinates for each source, μ_1 and μ_2, the logarithm of the background fraction, $\log f_{\mathrm{bkg}}$, and the logarithm of the count ratio, $\log f$. For both models, f_{bkg} is defined as the ratio of the number of counts associated with the background versus the number of counts associated with all point sources. For the dual-point-source model, f is defined as the ratio of the number of counts between the secondary and primary X-ray point source. For all priors, we use the standard ranges and distributions, as most recently detailed in B. Sandoval et al. (2024). All errors evaluated in the following subsection are done at the 95% confidence level.

Analysis of the data set with BAYMAX yields a Bayes Factor $\log \mathcal{BF} = 38 \pm 2$ in favor of the dual-point-source model. The position of the secondary X-ray point source coincides with the position of the additional emission component, and the best-fit separation and count ratio returned by BAYMAX are $r = 3\farcs3^{+0.3}_{-0.3}$ (approximately 2.4 kpc at $z = 0.0362$) and $\log f = -1.9^{+0.3}_{-0.3}$, respectively. The calculated position angle between the primary AGN (hereafter, MCG+11-11-032 X1, for simplicity) and the secondary X-ray point source (hereafter, MCG+11-11-032 X2, for simplicity) is $\mathrm{PA_X} = 149° \pm 4°$. This position angle is approximately perpendicular to the position angle of the galaxy's plane and the value where the two resolved narrow-emission-line peaks were previously determined to be maximally separated ($\mathrm{PA_{opt}} = 61°$; J. M. Comerford et al. 2012). Given that the best-fit coordinates of the two X-ray sources correspond to a separation over four times as large, and a position angle that is perpendicular to the values reported in J. M. Comerford et al. (2012), it is likely that this source is not the origin for the observed double-peaked [O III] emission lines. In Figure 2, we show the results from BAYMAX, including the best-fit locations of each X-ray point source on the Chandra image and the joint posterior distributions for r and $\log f$.

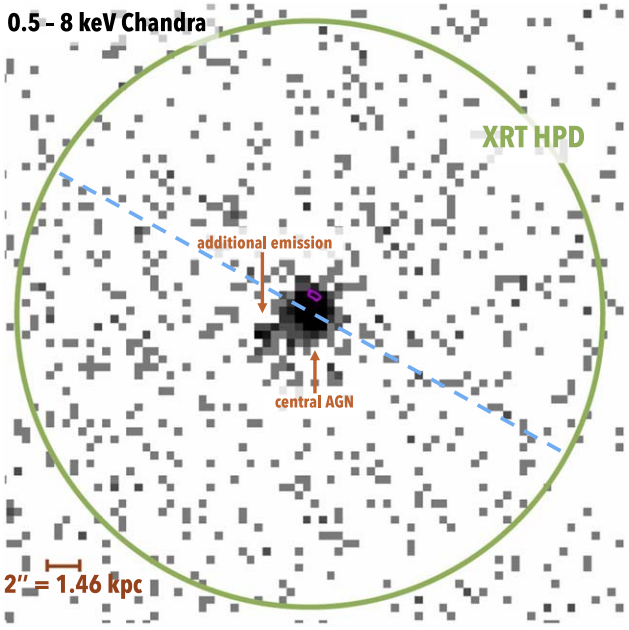

Figure 1. The 0.5–8 keV Chandra observation of MCG+11-11-032. The X-ray image has been binned to Chandra's native pixel resolution. In green, we show the Swift XRT half-power diameter at 1.5 keV (18″). The blue dashed line represents the position angle between the two [O III] λ5007 emission peaks on the sky ($\mathrm{PA_{opt}} = 61°$), as measured from the long-slit spectroscopy in J. M. Comerford et al. (2012); the absolute value of the difference between $\mathrm{PA_{opt}}$ and the isophotal position angle of the major axis from the SDSS r-band photometry is approximately $\mathrm{PA_{gal}}$ 14.°8. By eye, the observation shows additional X-ray emission centered >3″ away from the central AGN (orange arrow), with a position angle approximately perpendicular to the position angle measured for the two [O III] λ5007 emission peaks. The additional emission has a separation larger than the known artifact in Chandra's point-spread function, which is <1″ from the primary AGN, centered on its position (shown in magenta). North is up and east is to the left, and a 2″ bar (1.46 kpc at $z = 0.0362$) is shown for scale.

2.2. Binary AGN Hypothesis: Spectral Analysis of Chandra Data Set

The spectral analysis is performed by using the XSPEC 12.13.1 package (K. A. Arnaud 1996). We use Poisson likelihood statistics (cstat) to compare and determine the best-fit model (W. Cash 1979). When comparing two spectral models, a statistically significant improvement in the fit can be defined when $\Delta C_{\mathrm{stat}} > \Delta n_{\mathrm{fp}} \times 2.71$ (where Δn_{fp} represents the difference in the number of free parameters between the models: P. Tozzi et al. 2006; M. Brightman & Y. Ueda 2012), corresponding to a fit improvement with 90% confidence (M. Brightman et al. 2014). This criterion is consistent with the Akaike Information Criterion (AIC; H. Akaike 1974), a penalized likelihood with a penalty term that depends on the

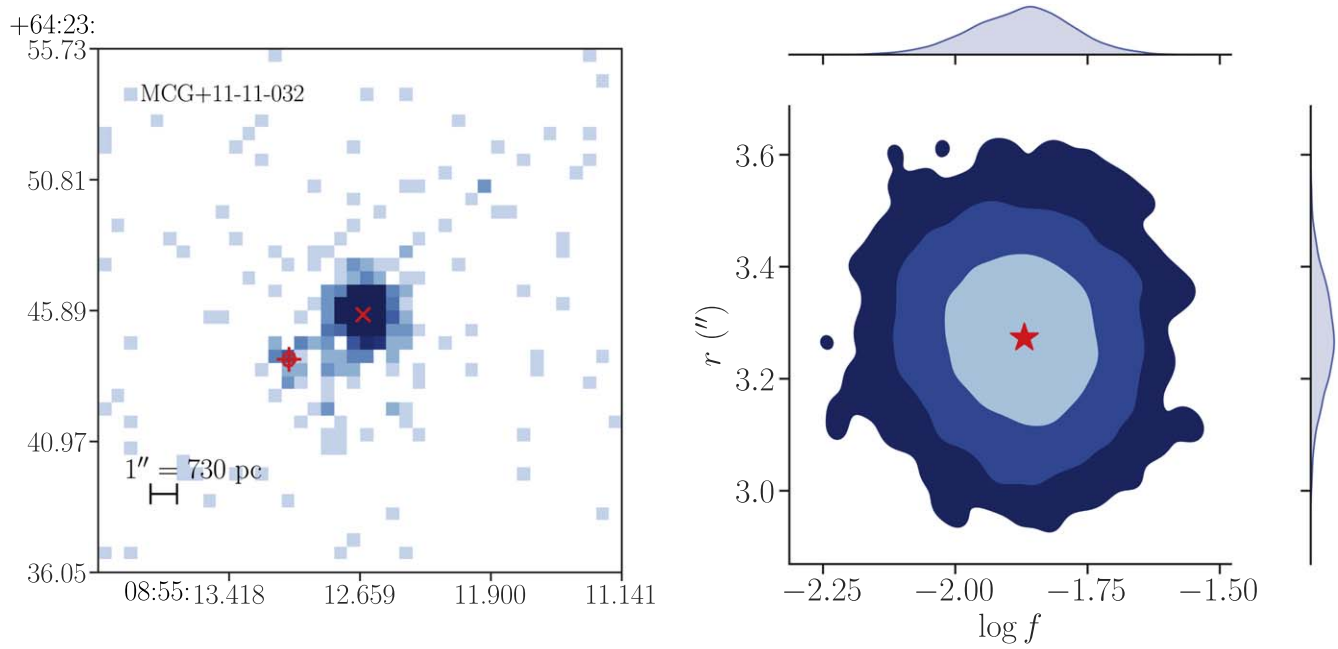

Figure 2. Results from BAYMAX showing the best-fit locations for the primary and secondary X-ray point sources over the 0.5–8 keV data set (left) and the joint posterior distributions for r and $\log f$ (right). In the left panel, we plot the 95% confidence intervals in red lines for the best-fit location, which are smaller than the symbol for the primary point source. The X-ray image has been binned to Chandra's native pixel resolution; north is up and east is to the left. In the right panel, the 68%, 95%, and 99.7% confidence intervals for r and $\log f$ are shown, from light to dark blue contours. We denote the location of the median of the posterior distributions with a red star.

number of free parameters in the model: $\Delta C_{\rm stat} > \Delta n_{\rm fp} \times 2.0$ (see J. Buchner et al. 2014 for use when comparing X-ray spectral models). This latter criterion ($C_{\rm AIC}$) has a lower threshold than the former and empirically defined criterion (C_{90}) but is rooted in information theory. We look at both criteria when evaluating the significance of adding different model components. The error bars quoted in the following section are calculated with Markov Chain Monte Carlo procedures via the XSPEC tool `chain` at the 95% confidence level for each parameter of interest. More details about the best-fit X-ray spectral parameters for each model described below can be found in Table 1.

We analyze the photons extracted within a 2″ radius circular region centered on the X-ray coordinates of MCG+11-11-032 and corresponding to 95% of the encircled energy radius at 1.5 keV for ACIS-S. For our background extraction, we use a source-free annulus with an inner radius of 10″ and outer radius of 20″. We calculate a count rate of approximately 6.31×10^{-2} cts s^{-1}, representing a state in between the low and high states observed with XRT (P. Severgnini et al. 2018). P. Severgnini et al. (2018) observed MCG+11-11-032 in both the low and high states and only fit the higher-state (and higher-statistics) spectrum, finding the best-fit model to be an intrinsically absorbed power law (`ztbabs*zpowerlw`) plus a continuum-reflection component (`pexrav`; P. Magdziarz & A. A. Zdziarski 1995) and a narrow-emission-line component (`zgaus`) that accounts for possible Fe Kα emission (`tbabs*(ztbabs*zpowerlw+pexrav+zgaus)`). The `pexrav` component was originally added due to both the soft- (<2 keV) and hard-energy (>6 keV) residuals when modeling the spectrum with an absorbed power law (suggesting the presence of a reflection component that may be due to, e.g., circumnuclear material).

Given that our Chandra observation represents a state in between the low and high states, we first fit our data using a simpler model composed of an intrinsically absorbed power law plus a continuum-reflection component (hereafter, Model 0: `tbabs*(ztbabs*zpowerlw+pexrav)`). We fix the photon index of the power law, Γ, to the photon index of the reflection component. We set the initial value of Γ to 1.8 and allow the value to vary between 1 and 3 (A. Corral et al. 2011; C.-S. Yan et al. 2015). We set the `pexrav` reflection scaling factor (`rel`) to a value of -1, such that it represents the reflection component only. We find a power-law slope Γ that is pegged at, and consistent with, the lower limit of 1, indicating a poor fit to the data.

For the most precise comparison to the results presented in P. Severgnini et al. (2018), we then adapt their best model: `tbabs*(ztbabs*zpowerlw+pexrav+zgaus)`—hereafter, Model 1. We set the initial line-energy value for the `zgaus` component to the best-fit value found in P. Severgnini et al. (2018; $E = 6.18$ keV), allowing the value to vary in the 6–7 keV energy range. Interestingly, P. Severgnini et al. (2018) find the emission-line component to be significantly lower (at the 97% confidence level) than the nominal rest-frame value for Fe Kα near ∼6.4 keV. This energy value has no clear association with the well-known and expected transitions in the X-ray band. Following P. Severgnini et al. (2018), we also freeze the σ value to 50 eV. We find best-fit values for the Gaussian emission component of $E = 6.4^{+0.3}_{-0.2}$ keV with equivalent width $EW = 66^{+60}_{-58}$ eV. The best-fit properties of the emission line are at a higher energy (that is consistent with the nominal rest-frame value for Fe Kα near ∼6.4 keV) and lower equivalent width than presented in P. Severgnini et al. (2018). However, similar to Model 0, we find a power-law slope Γ that is pegged at, and consistent with, the lower limit of 1. We find that Model 1 is statistically preferred to Model 0 using the $C_{\rm AIC}$ criterion but does not meet the C_{90} criterion. This may be driven by the fact that we are observing MCG+11-11-032 in a lower state than the XRT spectrum.

Table 1
X-Ray Spectral Properties of MCG+11-11-032

X-Ray Spectral Model Comparison: MCG+11-11-032 X1							
Model	Γ	N_H (10^{22} cm^{-2})	E (keV)	EW (eV)	$F_{2-10\ keV}$ (10^{-12} erg s^{-1} cm^{-2})	$L_{2-10\ keV}$ (10^{42} erg s^{-1})	C_{stat}/dof/n_{fp}
(1)	(2)	(3)	(4)	(5)	(6)	(7)	(8)
M0	$1.1^{+1.6}_{-0.1}$	$12.6^{+5.8}_{-1.0}$	N/A	N/A	$3.3^{+0.3}_{-0.3}$	$9.5^{+0.9}_{-0.9}$	540.5/507/5
M1	$1.1^{+0.7}_{-0.1}$	$12.6^{+4.6}_{-1.1}$	$6.4^{+0.3}_{-0.2}$	66^{+60}_{-58}	$3.3^{+0.2}_{-0.4}$	$9.4^{+0.5}_{-1.1}$	535.9/505/7
M2	$1.2^{+0.7}_{-0.2}$	$12.7^{+4.2}_{-1.2}$	$6.3^{+0.6}_{-0.3}$ $6.5^{+0.4}_{-0.5}$	67^{+59}_{-66} 130^{+72}_{-129}	$3.3^{+0.1}_{-0.3}$	$9.4^{+0.7}_{-0.7}$	535.7/503/9
M3	$1.1^{+1.9}_{-0.1}$	$12.7^{+87.3}_{-0.9}$	6.16 (fixed) 6.56 (fixed)	$<10^{-10}$ 9^{+300}_{-3}	$3.2^{+0.1}_{-0.4}$	$9.7^{+0.3}_{-1.0}$	540.4/505/7
M4	$1.4^{+0.8}_{-0.2}$	$13.6^{+5.1}_{-1.6}$	$6.4^{+0.3}_{-0.1}$ $7.6^{+0.1}_{-0.3}$	85^{+70}_{-71} 161^{+161}_{-95}	$3.2^{+0.3}_{-0.4}$	$9.4^{+0.8}_{-0.8}$	530.9/503/9
BAYMAX Best-fit Spectral Parameters: MCG+11-11-032 X1 and X2							
Source	Γ	N_H (10^{22} cm^{-2})	E (keV)	EW (eV)	$F_{2-10\ keV}$ (10^{-12} erg s^{-1} cm^{-2})	$L_{2-10\ keV}$ (10^{42} erg s^{-1})	HR
(1)	(2)	(3)	(4)	(5)	(6)	(7)	(8)
X1	$1.4^{+0.1}_{-0.1}$	$13.9^{+0.4}_{-0.4}$	$6.4^{+0.1}_{-0.1}$ $7.6^{+0.1}_{-0.1}$	55^{+6}_{-5} 162^{+17}_{-21}	$2.9^{+0.1}_{-0.1}$	$8.3^{+0.1}_{-0.1}$	$0.9^{+0.1}_{-0.1}$
X2	1.8 (fixed)	$9.4^{+10.3}_{-2.9}$			$3.0^{+0.7}_{-0.9} \times 10^{-2}$	$1.5^{+0.9}_{-0.5} \times 10^{-1}$	$0.9^{+0.1}_{-0.1}$

Note. Top. Column (1): spectral model used. Column (2): the best-fit spectral index. Column (3): the best-fit extragalactic column density. Column (4): the best-fit central line energy for the zgaus component. Column (5): the equivalent width measured for the zgaus component. Column (6): the measured 0.5–8 keV flux, in units of 10^{-12} erg s^{-1} cm^{-2}. Column (7): the rest-frame 2–10 keV luminosity, in units of 10^{42} erg s^{-1}. Column (8): the C_{stat}, degrees of freedom (dof), and n_{fp} values associated with each model and used to quantify the best fit (see the text for more details). Bottom. Column (1): source name. Column (2): the assumed or best-fit spectral index. Column (3): the best-fit extragalactic column density. Column (4): the best-fit central line energy for the zgaus component. Column (5): the best-fit equivalent width measured for the zgaus component. Column (6): the measured 0.5–8 keV flux, in units of 10^{-12} erg s^{-1} cm^{-2}. Column (7): the rest-frame 2–10 keV luminosity, in units of 10^{42} erg s^{-1}. Column (8): the HR (see the text for the definition). Each best-fit value is defined as the median of the full distribution (see the text for more details). For MCG+11-11-032 X2, Column (7) represents the unabsorbed luminosity, calculated using the XSPEC model component cflux.

Following the results presented in P. Severgnini et al. (2018), we test for the presence of two emission lines by adding a second (zgaus) component to our model. We set the initial line-energy values for both components to the best-fit values found when fitting the XRT data with two Gaussian components ($E_1 = 6.16$ keV and $E_2 = 6.56$ keV). We allow the values to vary in the 6–7 keV energy range and freeze the σ values to 50 eV (hereafter, Model 2). We find that this fit does not result in a statistically significant improvement to Model 1 using either the C_{90} or C_{AIC} criterion. This is unsurprising, given that the two emission lines are shifted from their initial values and centered at values consistent with the single Gaussian component in Model 1 ($E_1 = 6.3^{+0.6}_{-0.3}$ keV and $E_2 = 6.5^{+0.4}_{-0.5}$ keV). Similar to Model 1, the best-fit value for Γ is pegged at, and consistent with, our lower boundary of 1.

In an attempt to quantify the statistical significance of a model with two distinct emission lines, we fit the data using the same components as in Model 2 but freeze the line-energy values of both zgaus components to $E_1 = 6.16$ keV and $E_2 = 6.56$ keV (hereafter, Model 3). This fit does result in a statistically significant improvement. In particular, the normalizations of both emission lines are shifted to values a factor of 10 smaller than Model 2, such that the equivalent widths of each line are consistent with, or close to, 0. Similar to both Model 1 and Model 2, the best-fit value for Γ is pegged at, and consistent with, a value of 1.

The residuals between the data and the best-fit spectra for all of our models show an excess of emission between 7 and 8 keV. We fit the data using the same components in Model 2 but with initial line-energy values for each zgaus component of $E_1 = 6.4$ keV (allowed to vary between 6 and 7 keV) and $E_2 = 7.5$ keV (allowed to vary between 7 and 8 keV). We freeze the σ values to 50 eV (hereafter, Model 4). We find best-fit values for the Gaussian emission components of $E_1 = 6.4^{+0.3}_{-0.1}$ keV with an equivalent width EW $= 85^{+70}_{-71}$ eV and $E_2 = 7.6^{+0.1}_{-0.3}$ keV with EW $= 161^{+161}_{-95}$ eV. A second emission line near 7.5 keV can possibly be associated with either Fe Kβ, Ni Kα, or a combination of the two. With respect to Model 1, Model 4 is statistically preferred using the C_{AIC} criterion but does not meet the C_{90} criterion; however, Model 4 is the only model that results in a Γ value that is not pegged at the boundary value of 1. Thus, we conclude that Model 4 best describes the X-ray emission associated with MCG+11-11-032. We find no evidence of double-peaked narrow Fe Kα lines with an orbital velocity offset of $\Delta v \approx 0.06$ in the X-ray spectrum of MCG+11-11-032. In Figure 3, we show our best-fit model (Model 4) overplotted on the data.

3. Discussion

Regarding the dual AGN hypothesis, we find that the Chandra observation has an additional X-ray emission component (MCG+11-11-032 X2) approximately 3″ from

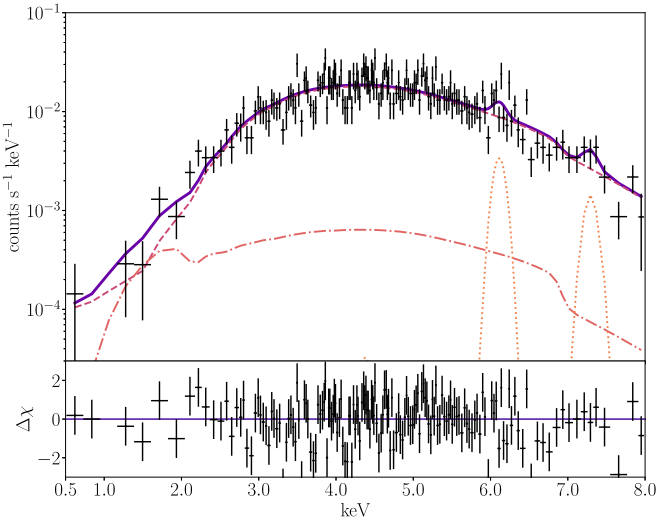

Figure 3. Top: spectrum of the central AGN shown in black, with the best-fit model overplotted in dark purple. We find that Model 4 results in the best fit, defined as: `tbabs*(ztbabs*zpowerlw+pexrav+zgaus+zgaus)`. We plot each component individually: `zpowerlw` with the pink dashed line, `pexrav` with the orange dotted–dashed line, and both `zgaus` components with the gold dotted line. We allow each `zgaus` component to vary between 6–7 keV and 7–8 keV and find best-fit values of $E_1 = 6.4^{+0.3}_{-0.1}$ keV with EW $= 85^{+70}_{-71}$ eV and $E_2 = 7.6^{+0.1}_{-0.3}$ keV with EW $= 161^{+161}_{-95}$ eV. We find no evidence of double-peaked narrow Fe Kα lines with an orbital velocity offset of $\Delta v \approx 0.06$ in the X-ray spectrum of MCG+11-11-032. The emission line at ≈7.5 keV can possibly be associated with either Fe Kβ, Ni Kα, or a combination of the two. Bottom: residuals between the data and model, defined as (data – model) / error, where the "error" is calculated as the square root of the model-predicted number of counts.

the central AGN (MCG+11-11-032 X1). However, we find that the position angle between MCG+11-11-032 X1 and X2 is perpendicular to the previously calculated position angle between resolved double-peaked narrow [O III] emission lines in the galaxy (J. M. Comerford et al. 2012). Regarding the binary AGN hypothesis, we find no strong evidence of double-peaked Fe Kα emission in the Chandra spectrum. In the following section, we further discuss possible origins of MCG +11-11-032 X2 and how it may have contaminated previous analyses searching for evidence of a binary AGN.

3.1. Possibility of Outflows in MCG+11-11-032

Importantly, our initial analysis with `BAYMAX` models the X-ray emission for any detected component as a point source, as expected for AGNs. Some of the emission associated with MCG+11-11-032 X2 may be due to the presence of an outflow. AGN outflows can interact with the host galaxy and surrounding medium, resulting in large-scale ionization detectable in both X-ray and optical wavelengths. Specifically, Seyfert 2 galaxies have shown soft (<3 keV) extended X-ray emission that is spatially correlated with O III emission, indicating that photoionization might be the common origin for these phenomena (S. Bianchi et al. 2006, 2010; N. A. Levenson et al. 2006; A. Travascio et al. 2021).

The observations of MCG+11-11-032 from the Blue Channel Spectrogram on the MMT 6.5 m telescope were re-analyzed in R. Nevin et al. (2016), as part of a study on 71 double-peaked narrow-emission-line sources. A kinematic classification scheme was used to classify each spectrum in order to determine the origin of the double-peaked [O III] emission. The majority (86%) of the sample was found to have [O III] profiles well described by moderate-luminosity AGN outflows. However, MCG+11-11-032 was classified as "ambiguous" (the smallest classification group, only 8% of the sample), given that the line-of-sight velocity and the dispersion of [O III] were not unambiguously associated with outflows (<400 km s^{-1} and <500 km s^{-1}, respectively) and that the [O III] emission was found to be misaligned with the galaxy plane. The extension of the [O III] emission was found to have a position angle of $PA_{opt} = 137°$, similar to the position angle determined from the X-ray analysis ($PA_X = 149° \pm 4°$).

We evaluate the Chandra observation for the presence of outflows by analyzing three energy bins: 0.5–2 keV (where emission associated with outflows may dominate); 2–3 keV; and 3–8 keV. In Figure 4, we show the filtered Chandra data. In the lowest-energy bin, we find evidence for extended soft emission (with extension on ∼4″ scales, or 2.9 kpc at $z = 0.0362$). The source appears to be dominated by <2 keV photons, as there is no evidence for extended emission in the 2–3 keV or 3–8 keV bands. In all energy bands, there exists a compact source at the coordinates of MCG+11-11-032 X2, as previously returned by `BAYMAX`. Within a 1″ extraction region centered on these coordinates, we calculate a hardness ratio (HR), defined as $(H - S)/(H + S)$, where H and S are the numbers of hard (2–8 keV) and soft (0.5–2 keV) X-ray counts, respectively. The HR value for a given source is independent of the model used to describe the source, and it can be used to identify the characteristics of a given emitter in the low-count regime. We find HR = 0.48, consistent with the values observed for type 2 AGNs across a range of expected extragalactic column densities (G. Hasinger 2008). Due to contamination from the soft extended region, the true value is likely higher.

We calculate the ratio of counts within a 1″ radius circle centered on the coordinates of MCG+11-11-032 X2 and MCG +11-11-032 X1, as a function of energy. We find the ratios to be consistent across all energy bins (≈0.1) and with our previous results obtained using `BAYMAX` ($\log f = -1.9$). The exception is in the 0.5–2 keV range (≈0.47), where contamination from the extended component is expected. Given the low number of counts associated with the soft extended component (≈12), it is challenging to constrain other properties, such as the position angle and spectrum. However, the soft extended X-ray component and the double-peaked narrow [O III] detected in MCG+11-11-032 reflect that large-scale emission around the nucleus of galaxy MCG+11-11-032 is multifaceted and may be partially composed of low-level outflows (although other X-ray contaminants that can contribute soft extended emission exist, including, e.g., star formation). We note that the kinematics powering the double-peaked [O III] emission in "ambiguous" sources is unclear: their spectra can be explained by many scenarios, including a counter-rotating disk caused by a merger, an outflow, an inflow, or some combination of these (R. Nevin et al. 2016).

To test the legitimacy of the assumption that MCG+11-11-032 X2 is a hard compact point source, separate from the soft extended X-ray emission observed near the nucleus, we carry out two analyses. The first is rerunning our analysis with `BAYMAX` as presented in Section 2.1, but on only the hardest photons in the observation (3–8 keV), to evaluate if the dual-point-source model remains favored over the single-point-source model; although we decrease the number of counts in the analysis by approximately 10% (and thus lose statistical

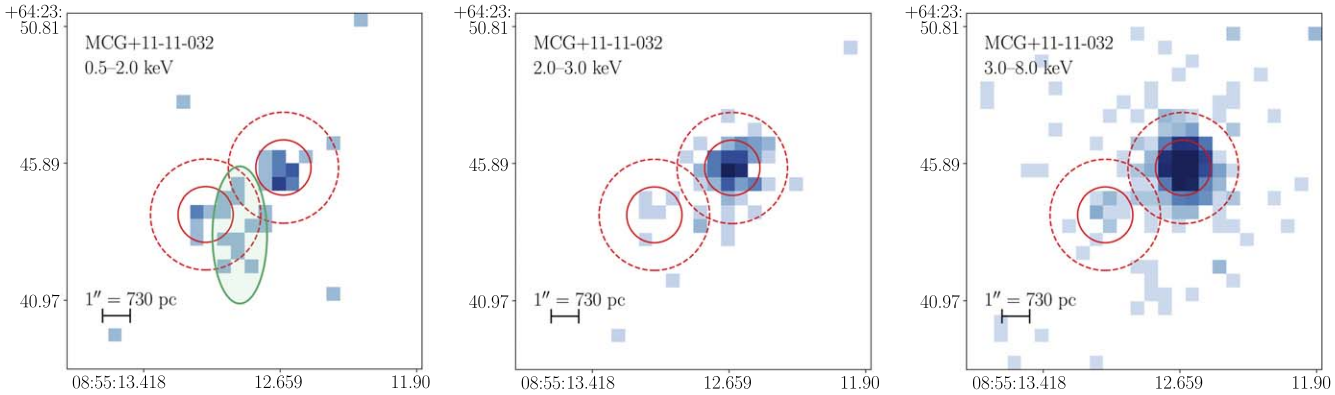

Figure 4. X-ray data of MCG+11-11-032 in different energy bins: 0.5–2 keV (left), 2–3 keV (center), and 3–8 keV (right). The X-ray images are binned to Chandra's native pixel resolution. With the solid (dashed) red lines, we plot 1″ (2″) radius circles centered on the best-fit location for the primary and secondary as determined by BAYMAX when analyzing the full 0.5–8 keV data set (see Section 2.1). In the lowest-energy bin, we find evidence for soft extended emission on ≈4″ scales, shown with a green ellipse. The source is dominated by photons with energies <2 keV, as we find no evidence for extended emission in the 2–3 keV or 3–8 keV bands. By eye, a compact source is observed at all energy bins, consistent with the location of the secondary point source as determined by BAYMAX. The majority of counts are contained within 1″, as expected for a point source. Furthermore, the ratio of counts within a 1″ radius around the coordinates of the secondary and primary is consistent across all energy bins (≈0.01) and with our previous results obtained using BAYMAX ($\log f = -1.9$). The exception is in the 0.5–2 keV range (0.47), where contamination from the extended emission is expected.

power), this energy range eliminates the majority of contamination associated with diffuse emission (see Figure 4). Our first analysis yields $\log \mathcal{BF} = 9.4 \pm 2$, in favor of the dual-point-source model. The position of the secondary X-ray point source is consistent with the results presented in Section 2.1, while the count ratio is marginally lower ($\log f \approx -2.1$; as expected, due to less contamination from the extended soft region). In Figure 7, we show the results from the 3–8 keV analysis with BAYMAX, where each count has been probabilistically assigned to a model component.

The second is rerunning our analysis on the 0.5–8 keV photons with BAYMAX, using updated models to quantify whether the dual-point-source model remains favored when including a diffuse emission region near the location of MCG +11-11-032 X2 (modeled as a component with a spatially uniform distribution of photons). In particular, it is possible that a spatially uniform component with a high count rate sitting among a spatially uniform background with a lower count rate can be mistaken for a secondary point source. We update our single and dual models to include an additional high-count and spatially uniform component. This component is defined within an elliptical region that covers the majority of the extended emission (as determined in the 0.5–2 keV range), with semimajor and semiminor axes of 5″ and 2″, respectively (see Figure 4). The region overlaps with 1″ of the best-fit location for MCG+11-11-032 X2, as determined in Section 2.1. Within this region, the background component is replaced with a spatially uniform emission component that has a different count rate than the background. This model component is parameterized by $f_{\rm diff}$, which represents the fraction of counts in the region that are associated with the diffuse high-count component. We include this parameter in both the single- and double-point-source models, with the goal of quantifying if a single point source plus a region of high-count-rate diffuse emission can statistically describe the data better than a model that includes a second point source.

We emphasize that because most of the extended X-ray emission is observed below 2 keV (see Figure 4), this analysis likely overestimates the contribution of the photons associated with the extended component. We find a Bayes factor value of $\log \mathcal{BF} = 28.6 \pm 2.2$, in favor of the dual-point-source model. In Figure 7, we show the results from this analysis, where each count has been probabilistically assigned to each model component. Even with an additional high-count component, we find strong evidence for the presence of a point source.

Thus, although both the X-ray and optical wave bands (R. Nevin et al. 2016) suggest that MCG+11-11-032 has low-level outflows, we find evidence of an additional compact and hard point source that sits approximately 3.″3 from the nucleus in MCG+11-11-032. Ground-based integral field unit (IFU) spectroscopy observations will allow for a much more detailed mapping of the optical ionization around the nucleus of MCG +11-11-032, including the extent, geometry, and spectrum.

3.2. X-Ray Spectral Analysis of MCG+11-11-032 X2

Assuming that MCG+11-11-032 X2 can be well represented as a point source, we investigate the origin of the emission by analyzing its X-ray spectrum. As outlined in A. Foord et al. (2020), BAYMAX can be used to carry out a spectral analysis of each detected point-source component. We use our best-fit results from the full energy band (0.5–8 keV) as presented in Section 2.1, with the caveat that we expect low-level contamination (fewer than 2 counts) in both the spectra of MCG+11-11-032 X1 and MCG+11-11-032 X2 at photon energies <2 keV from the extended soft source.

We create 100 spectral realizations of each component by probabilistically sampling from the full distribution of counts. Each spectral realization is associated with [μ_1, μ_2, $f_{\rm bkg}$, f] values that are drawn from the posterior distributions of the dual-point-source model. Each count is then assigned to a specific model component (i.e., the primary, secondary, or background), based on the respective probabilities of being associated with each component. On average, the secondary point source's spectrum only has 27 counts (as compared to the primary's average of 1965 counts), which limits the complexity of our spectral model. We fit each spectral realization of both point-source components with XSPEC; all of the spectral realizations of the primary point source (MCG+11-11-032 X1) are fit with the same constraints used in Model 4, while the secondary point source (MCG+11-11-032 X2) spectral

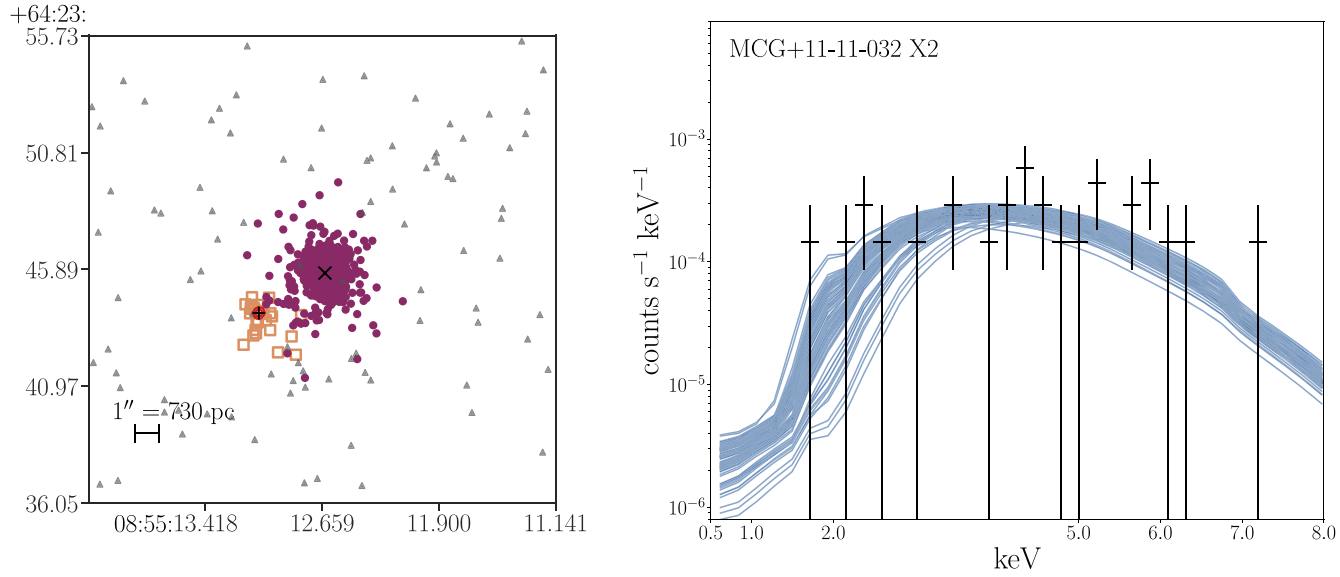

Figure 5. Left: the unbinned 0.5–8 keV data set for MCG+11-11-032, where BAYMAX has probabilistically assigned each count to a model component. Here, the counts most likely associated with the primary are denoted by the red circles, the counts most likely associated with the secondary are denoted by the open-faced orange squares, and the counts most likely associated with the background are shown as the gray triangles. Right: X-ray spectral fits of 100 realizations for the secondary point source (MCG+11-11-032 X2) in MCG+11-11-032. Data have been folded through the instrument response. We overplot one of the spectral realizations in black. The spectra have been rebinned for plotting purposes.

realizations are fit with an absorbed power law (`tbabs*(ztbabs*zpowerlw)`), with a fixed photon index $\Gamma = 1.8$.

We analyze the distributions of the best-fit values for each spectral parameter and the 2–10 keV flux and luminosity. We define the best-fit value for a given spectral parameter as the median of the distribution of values and calculate the 99.7% confidence intervals to estimate the errors. Figure 5 shows an example of the X-ray photons probabilistically assigned to either MCG+11-11-032 X1 or MCG+11-11-032 X2 for one of the realizations.

In Table 1, we list the best-fit spectral values returned by our spectral analysis with BAYMAX. For MCG+11-11-032 X1, we find the distributions for Γ, $N_{\rm H}$, $F_{2-10\,\rm keV}$, $L_{2-10\,\rm keV}$, and parameters associated with both emission lines consistent with the previously calculated best-fit parameters when fitting the extracted spectrum with Model 4. The larger error bars associated with certain parameters from our analysis in Section 2.2 may be due to possible contamination from MCG +11-11-032 X2 when extracting counts within a 2″ region centered on MCG+11-11-032 X1. For MCG+11-11-032 X2, we find the following best-fit spectral parameters: $N_{\rm H} = 9.4^{+10.3}_{-2.9} \times 10^{22}\,\rm cm^{-2}$, $F_{2-10\,\rm keV} = 3.0^{+0.7}_{-0.9} \times 10^{-14}\,\rm erg\,s^{-1}\,cm^{-2}$, and unabsorbed $L_{2-10\,\rm keV} = 1.5^{+0.9}_{-0.5} \times 10^{41}\,\rm erg\,s^{-1}$ (assuming the same redshift as MCG+11-11-032). Interestingly, the secondary is relatively luminous, nearing the nominal threshold above that classifies persistent X-ray sources as bona fide AGNs ($L_{2-10\,\rm keV} \sim 10^{41}$–$10^{42}\,\rm erg\,s^{-1}$; S. Fotopoulou et al. 2016; B. D. Lehmer et al. 2019). We calculate $\rm HR = 0.9^{+0.1}_{-0.1}$ and $\rm HR = 0.9^{+0.1}_{-0.1}$ for MCG+11-11-032 X1 and X2, respectively.

3.3. Multiwavelength Coverage of MCG+11-11-032

To better understand the possible origin of the emission for MCG+11-11-032 X2, we analyze the available archival multiwavelength data of the host galaxy. In the optical and infrared there exists SDSS *u*, *g*, *r*, *i*, *z* coverage; and Hubble Space Telescope (HST) WFC3/IR F105W ($\lambda_{\rm eff} = 1.04\,\mu$m), WFC3/UVIS F547M ($\lambda_{\rm eff} = 5436$ Å), and WFC3/UVIS F621M ($\lambda_{\rm eff} = 6209$ Å) coverage (PropID: 12521; PI: Liu). The radio regime includes the Very Large Array (VLA) Sky Survey (2–4 GHz; R. A. Perley et al. 2011), the VLA Faint Images of the Radio Sky at Twenty-Centimeters survey (1.4 GHz; R. H. Becker et al. 1995), *X*-band VLA observations (8–12 GHz; ProjectID: 13B-020; PI: Comerford), and the LOw-Frequency ARray (LOFAR) Two-meter Sky Survey (LoTSS) DR2 (120–168 MHz; T. W. Shimwell et al. 2022).

We find no evidence of an optical counterpart in the SDSS data sets. However, this is not unexpected, given the typical resolution of SDSS (∼1.″5) and the fact that the projected position of MCG+11-11-032 X2 is coincident with a relatively dense region of the edge-on spiral galaxy, with a highly obscured line of sight. Within the HST data, all three bands resolve a point source that is coincident with the X-ray coordinates of MCG+11-11-032 X2. We note that the level of intrinsic absorption in the spectrum of MCG+11-11-032 X2 is relatively high, on the order of $\sim 10^{23}\,\rm cm^{-2}$. If the object powering MCG+11-11-032 X2 is also powering the off-nuclear detection in the HST F105W/F621M/F547M data, it is likely that these levels of absorption are circumnuclear. Although the source may sit within a highly obscured line of sight, the estimated level of dust attenuation in the *V* band ($A_V = 1.044$ mag; S. Salim et al. 2018) cannot account for the level of measured $N_{\rm H}$ alone (e.g., P. Predehl & J. H. M. M. Schmitt 1995). In Figure 6, we show SDSS *r*-band, HST F105W, and HST F47M/F621M images.

We find a faint 3.3σ noise bump in both VLA survey maps at the coordinates of MCG+11-11-032, but given the low significance of the signal we cannot confidently attribute the emission to MCG+11-11-032. Analysis of the *X*-band VLA observations yields a nondetection at the location of MCG+11-11-032, resulting in an upper limit on the *X*-band flux density of approximately 0.13 mJy. Within LoTSS DR2, we find an $\sim 8\sigma$ detection at the

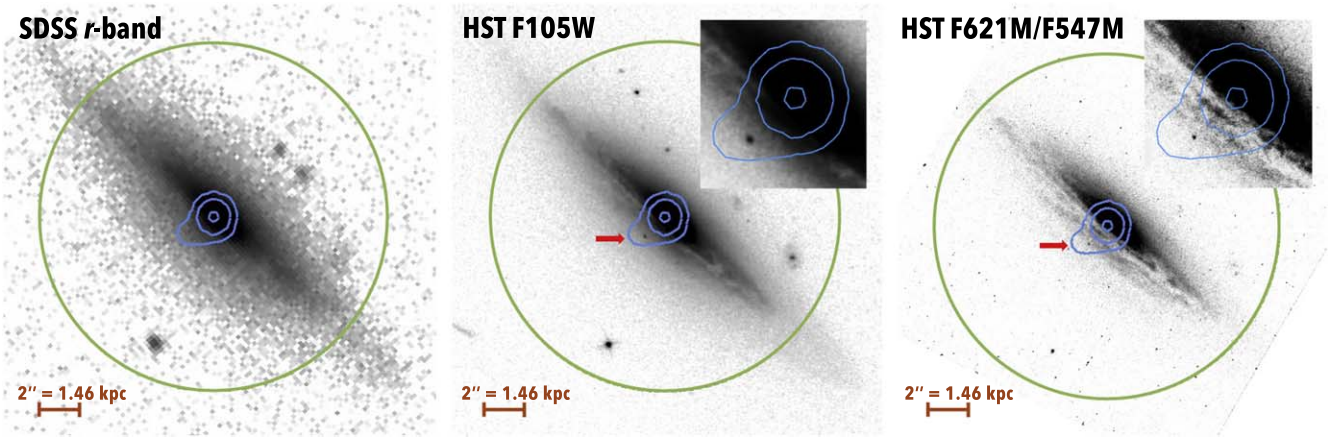

Figure 6. SDSS *r*-band (left), HST WFC3/IR 105W (center), and combined HST WFC3/UVIS F574M/F621M (right) coverage of MCG+11-11-032. The insets for both the center and right panels show a zoomed-in field of view of the nucleus of MCG+11-11-032. In green, we show the Swift XRT half-power diameter at 1.5 keV (18″), which covers the majority of the observable optical light associated with MCG+11-11-032. In blue, we show contours of the 0.5–8 keV Chandra emission, with the southeast extension due to the presence of MCG+11-11-032 X2. We find no evidence of an optical counterpart in the SDSS data set. Within the HST data, all three bands resolve a point source that is coincident with the X-ray coordinates of MCG+11-11-032 (shown with a red arrow). North is up and east is to the left, and a 2″ bar (1.46 kpc at $z = 0.0362$) is shown to scale.

coordinates of MCG+11-11-032, with a peak flux density of 2.42 mJy beam^{-1}. Given the angular resolution of the survey (6″), the radio detection can be associated with either (or both) of the X-ray point sources. We convert the radio flux density from the LOFAR band to 5 GHz ($S_{5\,\mathrm{GHz}}$) by assuming a spectral index of $\alpha = 0.7$ (adapting the sign convention $S_\nu \propto \nu^{-\alpha}$), which represents the median spectral index value for AGNs in LOFAR surveys (G. Calistro Rivera et al. 2017). We estimate a 5 GHz flux density of $S_{5\,\mathrm{GHz}} = 0.21$ mJy, consistent with a nondetection in both VLA survey maps (<0.5 mJ at 5 GHz) and the *X*-band upper limit of 0.13 mJy at 10 GHz.

3.4. A Candidate Hyperluminous X-Ray Source

Given that the X-ray emission of MCG+11-11-032 X2 appears to be off-nuclear, and is relatively luminous, it may originate from an ultraluminous X-ray source (ULX). ULXs are generally defined as off-nuclear and luminous ($L_X > 10^{39}$ erg s^{-1}) sources that are distinct from the galaxy's central SMBH (see the reviews presented in P. Kaaret et al. 2017; A. King et al. 2023 and references therein). There are various theoretical explanations for the observed emission, the most common being super-Eddington stellar remnants ($M < 10M_\odot$). The super-Eddington accretion has been explained via many models, including the presence of strong magnetic fields (e.g., V. Canuto & C. K. Chou 1971; M. M. Basko & R. A. Sunyaev 1976; M. Bachetti et al. 2014; K. Y. Eksi et al. 2015; A. A. Mushtukov et al. 2015; S. S. Tsygankov et al. 2016); geometric beaming (A. R. King et al. 2001; J. Poutanen et al. 2007; M. J. Middleton et al. 2015); and "leaky disks" (M. C. Begelman 2002). However, the majority of these models predict luminosities $L_X \lesssim 3 \times 10^{40}$ erg s^{-1}.

Ever rarer are sources with luminosities above the X-ray luminosity break of star-forming galaxies near $\approx 10^{41}$ erg s^{-1} (S. Mineo et al. 2012), classified as hyperluminous X-ray sources (HLXs; Y. Gao et al. 2003; H. Matsumoto et al. 2003). For objects with X-ray luminosities above 10^{41} erg s^{-1}, it is believed that the accretor can be explained by sub-Eddington intermediate-mass black holes (IMBHs; E. J. M. Colbert & R. F. Mushotzky 1999; Y. Taniguchi et al. 2000; J. M. Miller et al. 2004; T. E. Strohmayer & R. F. Mushotzky 2009; M. Mezcua 2017; R. S. Barrows et al. 2019, 2024; J. E. Greene et al. 2020), where $10^2 M_\odot \lesssim M_{\mathrm{BH}} \lesssim 10^5 M_\odot$. HLXs are rare in the local Universe (Y. Gao et al. 2003; A. D. Sutton et al. 2012; H. Gong et al. 2016; I. Zolotukhin et al. 2016), and searches are hampered by high levels of contamination from foreground stars and background AGNs (A. D. Sutton et al. 2015; I. Zolotukhin et al. 2016).

The strongest candidate for an HLX powered by a massive black hole is ESO 243-49 HLX-1. It has a peak X-ray luminosity of 10^{42} erg s^{-1} and sits approximately 8″ (3.7 kpc at $z = 0.023$) from the nucleus of the edge-on S0 galaxy ESO 243-49 (S. A. Farrell et al. 2009). HLX-1 was shown to be associated with the galaxy using optical spectroscopy (R. Soria et al. 2010), which detected a Balmer Hα emission line consistent with the redshift of the host galaxy (K. Wiersema et al. 2010; R. Soria et al. 2013). Multiwavelength photometric and spectroscopic coverage of ESO 243-49 HLX-1 has allowed for various (albeit relatively unconstrained) estimates of the black hole mass, ranging from $M_{\mathrm{BH}} \approx 10^4 M_\odot$ (S. W. Davis et al. 2011; M. Servillat et al. 2011; O. Godet et al. 2012; O. Straub et al. 2014) to $M_{\mathrm{BH}} < 2.9 \times 10^8 M_\odot$ (A. Merloni et al. 2003; D. Cseh et al. 2015; N. A. Webb et al. 2017). This range folds in the relatively large error bars associated with the mass estimates; and the upper end is likely overestimated, given that the X-ray emission appears to be extended and may include contaminants such as diffuse gas around the central source. It has been proposed that HLX-1 is an IMBH associated with a tidally stripped dwarf satellite galaxy (N. A. Webb et al. 2010; S. A. Farrell et al. 2012; R. Soria et al. 2013), although analyses of the environment around ESO 243-49 have found no evidence of signatures associated with a recent merger event (A. Musaeva et al. 2015; N. A. Webb et al. 2017).

If the radio detection in LoTSS DR2 originates from MCG +11-11-032 X1, we may expect that the mass estimated from the "fundamental plane of black hole activity" (FP; A. Merloni et al. 2003) is consistent with the mass of the AGN determined from the CO velocity dispersion of $\log M_{\mathrm{BH}}/M_\odot = 8.7 \pm 0.3$ (I. Lamperti et al. 2017). The FP is an empirical correlation between the mass of a black hole (M), the 5 GHz radio continuum luminosity (L_R), and the 2–10 keV X-ray luminosity

(L_X), reflecting the physical connection between the accretion, outflows, and mass. Offsets from the FP may be expected if the LOFAR detection consists of two radio emitters or if the LOFAR detection is dominated by radio emission associated with MCG+11-11-032 X2. In the first scenario, we may expect to observe an excess of radio emission with respect to the X-ray luminosity of MCG+11-11-032 X1, resulting in a projected mass that is larger than the previously measured value. In the second scenario, we may expect to observe a lower radio luminosity than necessary to meet the previously measured mass of MCG+11-11-032 X1.

We calculate a 5 GHz radio luminosity of $L_R = 3.1 \times 10^{37}$ erg s^{-1} using our previously derived value for $S_{5\,\mathrm{GHz}}$. Pairing this with our estimated X-ray luminosity for MCG+11-11-032 X1, we use the results of K. Gültekin et al. (2019) to calculate a projected mass for MCG+11-11-032 X1 of $\log M_{\mathrm{BH}}/M_{\odot} = 6.3^{+0.7}_{-0.7}$, a value significantly lower than the measured mass. We note that it is unclear if the FP relation is appropriate for systems that are not in a low/hard state, such as Seyferts like MCG+11-11-032 X1. In particular, high-accretion-rate AGNs with radiatively efficient disks likely have quenched their jets, and the detected radio emission may be residual from an earlier low/hard state of activity. However, past analyses reflect that the FP may be applicable for high-accretion-rate sources (e.g., F. Panessa et al. 2007; M. Giroletti & F. Panessa 2009; K. Gültekin et al. 2014). With this caveat in mind, we use the FP relation presented in K. Gültekin et al. (2019) derived using only Seyferts (see their Equation (15)). The scatter associated with the FP for Seyferts is larger, likely driven by only having seven Seyferts in their full sample; however, the FP relation for Seyferts versus the full sample remains consistent within $\sim 2\sigma$. We find $\log M_{\mathrm{BH}}/M_{\odot} = 5.8^{+1.8}_{-0.6}$, consistent (albeit with larger error bars) with the previous FP mass projection. If we assume that the majority of the radio flux originates from MCG+11-11-032 X2, and use our estimated X-ray luminosity for the source (see Section 3.1), we find $\log M_{\mathrm{BH}}/M_{\odot} = 7.3^{+0.4}_{-0.4}$. This value is consistent with the range of masses estimated for HLX-1 using the FP. Previous analyses that resolve the radio emission around ULXs have shown that the radio luminosity can include contributions from large-scale (lobe-like) and small-scale (jet) structures, resulting in FP projected masses that are biased toward higher values (M. Mezcua et al. 2015).

To further investigate the HLX hypothesis, we calculate the ratio of the extrapolated 5 GHz luminosity to the X-ray luminosity, $\log R_X$ (Y. Terashima & A. S. Wilson 2003). This ratio has an advantage over standard optical-to-X-ray ratios, in that it can be measured for highly absorbed nuclei ($N_H \gtrapprox 10^{23}$ cm^2). The value of this ratio has been measured to vary for compact objects as a function of their mass and has been used to flag potential IMBHs (e.g., the ULX IMBH candidate NGC2276-3c; see M. Mezcua et al. 2013, 2015). In particular, IMBHs may be expected to have values in between XRBs ($\log R_X < -5.3$) and low-luminosity AGNs ($-3.8 < \log R_X < -2.8$; M. Mezcua et al. 2013). Once again assuming that most of the radio emission is associated with either MCG+11-11-032 X1 or X2, we calculate $\log R_X$ values of -5.4 and -3.7, respectively. MCG+11-11-032 X1 has a value consistent with XRBs, at odds with its known AGN nature, while MCG+11-11-032 X2 has a value at the lower end of the AGN range. This may be further proof that the radio emission originates from MCG+11-11-032 X2 and that the source is powered by an IMBH. However, given the unknown relation between the radio and X-ray emission for Seyferts, and thus the unknown expected contribution from MCG+11-11-032 X1 in the LOFAR observation, we cannot rule out the possibility that the radio emission is associated with the central AGN.

Last, we also consider a simplified approach to estimating the mass of MCG+11-11-032 X2. Given that the source is fit with a spectrum in a low/hard state $\Gamma = 1.8$, we assume that the source is accreting at $\sim$1% Eddington (see, e.g., T. J. Maccarone 2003, 2005). We further assume the hard-X-ray bolometric correction $L_{\mathrm{bol}}/L_{2-10}$ for an Eddington ratio of $\lambda = 0.01$ is $\sim$2 (measured for a sample of ULXs; K. Anastasopoulou et al. 2022). We note that this bolometric correction is consistent with previous measurements for type 2 AGNs (e.g., E. Lusso et al. 2012). Using the estimated 2–10 keV luminosity of for X2 (see Table 1), we calculate a mass of $\sim 2.4 \times 10^5 M_{\odot}$, indicating a fairly low-mass black hole or an intermediate high-mass black hole.

Perhaps the strongest line of evidence for an HLX origin for MCG+11-11-032 X2 would be the detection of variability in its X-ray luminosity, as the majority of the strongest HLX candidates show evidence of variability on timescales of $\sim$months to a year (A. Wolter et al. 2006; P. Kaaret & H. Feng 2007; F. Pizzolato et al. 2010; J. P. Lasota et al. 2011; A. D. Sutton et al. 2012; D. R. Pasham & T. E. Strohmayer 2013). In particular, HLX-1 has been shown to mimic sub-Eddington black hole binaries on the hardness–intensity diagram as it progresses through periodic outbursts (M. Servillat et al. 2011). Given (1) the low number of counts, (2) the resulting unconstrained X-ray spectrum, and (3) our single-epoch Chandra observation, we do not currently have the ability to investigate whether the X-ray emission of MCG +11-11-032 X2 and its variability (or lack thereof) is consistent with other HLX candidates. If MCG+11-11-032 X2 does indeed undergo periodic outbursts, it may be driving the previous claims of a $\sim$25 month periodic behavior in the BAT light curve (P. Severgnini et al. 2018). However, because the BAT aperture includes both X-ray point sources, it is unclear how their individual behaviors would manifest in a joint light curve. Future modeling of the light curve will need to account for two potentially varying X-ray sources.

3.5. Alternative Hypotheses

Other origins of the emission for MCG+11-11-032 X2 include a background AGN. This type of contamination has been proven as the true origin of emission for a previously identified HLX candidate in IC 4320, 2XMM J134404.1-271410. With a measured X-ray luminosity of $L_X \approx 3.5 \times 10^{41}$ erg s^{-1} (assuming the same redshift as IC 4320), it was the second-most-luminous HLX candidate detected (A. D. Sutton et al. 2012). A compact and red counterpart was detected in Very Large Telescope (VLT) VIsible MultiObject Spectrograph data, and VLT FOcal Reducer/low dispersion Spectrograph 2 long-slit spectroscopy proved the source was a background QSO at $z = 2.84$ (A. D. Sutton et al. 2015). Using the $\log N - \log S$ cumulative number density of cosmic X-ray background sources from deep-field surveys (F. E. Bauer et al. 2004), we quantify the probability that MCG+11-11-032 X2 is a background source. We find the probability of background contamination within a 3.″3 radius around the center of MCG +11-11-032 is negligible ($P = 8 \times 10^{-3}$%). We note that a

similar type of analysis carried out for 2XMM J134404.1-271410, which sits 18″ from the center of IC 4320, yields a significantly higher probability ($P \sim 0.3\%$). By crudely categorizing the possibilities into two bins—either a background AGN or an HLX—the background contamination probability corresponds to a 3.8σ significance of MCG+11-11-032 X2 being an HLX (assuming a normal distribution). While this significance is not exceptionally high, it stands in stark contrast to the result for 2XMM J134404.1-271410, where a similar analysis yields a significance of only 0.5σ, underscoring the much lower level of confidence in its classification as an HLX. An analysis of the optical spectrum is necessary to confidently rule out contamination from a background QSO. Last, we note that MCG+11-11-032 X2 is likely not associated with a jet, given the coincident point-like sources detected in Chandra and HST. No other evidence for jet morphology is resolved in the available SDSS and HST images. However, higher-resolution radio coverage can provide better insight as to whether the properties of MCG+11-11-032 X2 are consistent with a jet.

4. Conclusions

In this study, we present an X-ray analysis of MCG+11-11-032. Using new Chandra observations, we investigate two hypotheses for both a binary (at subparsec separations) and a dual (separated by 0.″77) AGN in the nucleus of MCG+11-11-032. Chandra observations uniquely allow for resolving any two AGNs in a dual system and/or confirming the presence of any two narrow Fe emission lines at ∼6.4 keV in a binary system. Additionally, new Chandra observations allow for further unexpected discoveries. Multiwavelength data provided by SDSS, HST, VLA, and LOFAR enable a comprehensive analysis of any X-ray detections. The main results of this study are summarized below:

1. Analysis of the data set with BAYMAX yields a Bayes Factor $\log \mathcal{BF} = 38 \pm 2$ in favor of the dual-point-source model. The position of the secondary X-ray point source—MCG+11-11-032 X2—coincides with the position of a visibly identified additional X-ray component, and the best-fit separation and count ratio returned by BAYMAX are $r = 3.''3^{+0.3}_{-0.3}$ (approximately 2.7 kpc at $z = 0.0362$) and $\log f = -1.9^{+0.3}_{-0.3}$, respectively. The calculated position angle between the two point sources is $\mathrm{PA_X} = 149° \pm 4°$, which is approximately perpendicular to the position angle of the galaxy's plane. Given that the best-fit coordinates of the two X-ray sources correspond to a separation over four times as large than, and a position angle that is perpendicular to, the values previously reported in J. M. Comerford et al. (2012), it is unlikely that this source is the origin for the observed double-peaked [O III] emission lines.
2. We find no evidence of double-peaked narrow Fe Kα lines with an orbital velocity offset of $\Delta v \approx 0.06$ in the X-ray spectrum of MCG+11-11-032. The X-ray spectrum is best fit by an absorbed power law with two emission lines: a single Fe Kα line centered at $6.4^{+0.3}_{-0.1}$ keV and an emission line centered at $7.6^{+0.1}_{-0.3}$ keV, which can possibly be associated with either Fe Kβ, Ni Kα, or a combination of the two. We conclude that the Chandra data do not support the binary AGN interpretation.
3. Further investigation of the Chandra observation shows evidence for soft extended X-ray emission at energies <2 keV and angular scales ≈4″. However, given the low number of counts associated with this component (∼12), it is difficult to accurately constrain the geometry and spectrum. We test the legitimacy of the assumption that MCG+11-11-032 X2 is a hard compact point source, separate from the soft extended X-ray emission, via two analyses: rerunning BAYMAX on only the hardest photons (3–8 keV) and rerunning BAYMAX using updated models that account for an additional high-count diffuse emission component. Both tests yield strong evidence in favor of the dual-point-source model.
4. We use the results from BAYMAX to carry out a spatially resolved and statistical spectral analysis of both the central AGN (MCG+11-11-032 X1) and the secondary X-ray point source (MCG+11-11-032 X2). On average, the spectrum MCG+11-11-032 X2 only has 27 counts between 0.5 and 8 keV, while MCG+11-11-032 X1 has 1965. For MCG+11-11-032 X2, we find the following best-fit spectral parameters: $N_{\mathrm{H}} = 9.4^{+10.3}_{-2.9} \times 10^{22}\,\mathrm{cm^{-2}}$, $F_{2\text{–}10\,\mathrm{keV}} = 3.0^{+0.7}_{-0.9} \times 10^{-14}\,\mathrm{erg\,s^{-1}\,cm^{-2}}$, and unabsorbed $L_{2\text{–}10\,\mathrm{keV}} = 1.5^{+0.9}_{-0.5} \times 10^{41}\,\mathrm{erg\,s^{-1}}$ (assuming the same redshift as MCG+11-11-032 X1). Interestingly, the secondary is relatively luminous, nearing the nominal threshold above which persistent X-ray sources are classified as bona fide AGNs ($L_{2\text{–}10\,\mathrm{keV}} \sim 10^{41}$–$10^{42}\,\mathrm{erg\,s^{-1}}$).
5. HST imaging in the IR F105W ($\lambda_{\mathrm{eff}} = 1.04\,\mu$m) and optical F621M/F547M ($\lambda_{\mathrm{eff}} = 6209$ Å and $\lambda_{\mathrm{eff}} = 5436$ Å, respectively) bands resolves a point source that is coincident with the X-ray coordinates of MCG+11-11-032 X2. If MCG+11-11-032 X2 powers the emission detected in both HST and Chandra observations, it may be an HLX.
6. We find an 8σ LOFAR detection from the LoTSS DR2 survey at the coordinates of MCG+11-11-032. Assuming the radio emission is dominated by the central AGN, the FP predicts a projected mass that is inconsistent with, and significantly lower than, the previously constrained mass of the central AGN. Additionally, we calculate a radio-to-X-ray ratio $\log R_{\mathrm{X}} = -5.4$, consistent with an XRB and at odds with its known AGN nature. However, if the radio emission is dominated by MCG+11-11-032 X2, the FP estimates a projected mass of $\log M/M_{\odot} = 6.3^{+0.7}_{-0.7}$, consistent with the estimated mass for the best IMBH/HLX candidate to date, HLX-1. Additionally, we calculate a radio-to-X-ray ratio of $\log R_{\mathrm{X}} = -3.7$, a value consistent with the lower end of the AGN range. We note that a spatially resolved optical spectrum of the source is necessary to confidently rule out contamination from a background QSO.

Further data that could support the hypothesis that the emission of MCG+11-11-032 X2 is associated with an HLX include: (1) a spatially resolved optical spectrum of MCG+11-11-032 X2 that confirms its association with the galaxy MCG +11-11-032; (2) high-resolution and deep radio observations that can spatially resolve the radio emission around MCG+11-11-032 X1 and X2; and (3) the detection of X-ray variability on timescales of months associated with varying spectral hardness. Regarding (1) and (2), planned follow-up observations with ground-based observatories, such as the VLA, and IFU spectrographs, such as the Multi-Unit Spectroscopic Explorer,

will better constrain the origin of the X-ray emission associated with MCG+11-11-032 X2. Regarding (3), the Chandra X-ray observatory is the sole telescope that can resolve sources separated on scales $<6''$ and generate an individual light curve for MCG+11-11-032 X2. We emphasize that the detection of MCG+11-11-032 X2 was only possible due to Chandra's superb angular resolution, highlighting how previous binary AGN interpretations from larger-aperture instruments, such as Swift, need careful evaluation and further follow-up. This is one of many examples where high spatial resolution in the X-ray band is extremely important; wide-field-of-view but lower-angular-resolution X-ray imagers are not best suited to complementing the current and near-future fleet of NASA observatories with subarcsecond spatial resolution, such as the James Webb Space Telescope and the Nancy Grace Roman Space Telescope. It may not be until the early to mid 2030s that we will have access to another high-resolution X-ray imager, such as the Advanced X-ray Imagining Satellite (C. S. Reynolds et al. 2023), which will allow us to resolve closely separated compact objects.

Acknowledgments

This paper employs a list of Chandra data sets, obtained by the Chandra X-ray Observatory, contained in doi:10.25574/cdc.335. F.C. acknowledges the CXC grant associated with proposal number 23700236. The National Radio Astronomy Observatory is a facility of the National Science Foundation operated under cooperative agreement by Associated Universities, Inc.

The HST data presented in this article were obtained from the Mikulski Archive for Space Telescopes (MAST) at the Space Telescope Science Institute. The specific observations analyzed can be accessed via doi:10.17909/3xyk-1f32.

Basic research in radio astronomy at the U.S. Naval Research Laboratory is supported by 6.1 Base Funding. M. M. acknowledges support from the Spanish Ministry of Science and Innovation through the project PID2021-124243NB-C22. This work was partially supported by the program Unidad de Excelencia Maria de Maeztu CEX2020-001058-M. F.M.-S. acknowledges support from NASA through ADAP award 80NSSC19K1096.

Facilities: CXO, Sloan, HST, LOFAR.

Software: `CIAO` (v4.12; A. Fruscione et al. 2006), XSPEC (v12.13.1; K. A. Arnaud 1996), `nestle` (https://github.com/kbarbary/nestle), `PyMC` (J. Salvatier et al. 2016), `MARX` (v5.3.3; J. E. Davis et al. 2012).

Appendix

As noted in Section 3.1, we carry out two additional analyses to test the legitimacy of the assumption that MCG+11-11-032 X2 is a hard compact point source. First, we rerun our analysis with `BAYMAX` as presented in Section 2.1, but on only the hardest photons in the observation (3–8 keV) to evaluate if the dual-point-source model remains favored over the single-point-source model; second, we rerun our analysis on the 0.5–8 keV photons with `BAYMAX` using updated models to quantify whether the dual-point-source model remains favored when including a diffuse emission region near the location of MCG +11-11-032 X2 (modeled as a component with a spatially uniform distribution of photons). Both tests yield Bayes factors values in favor of the dual-point-source model. In Figure 7, we show the results from these tests.

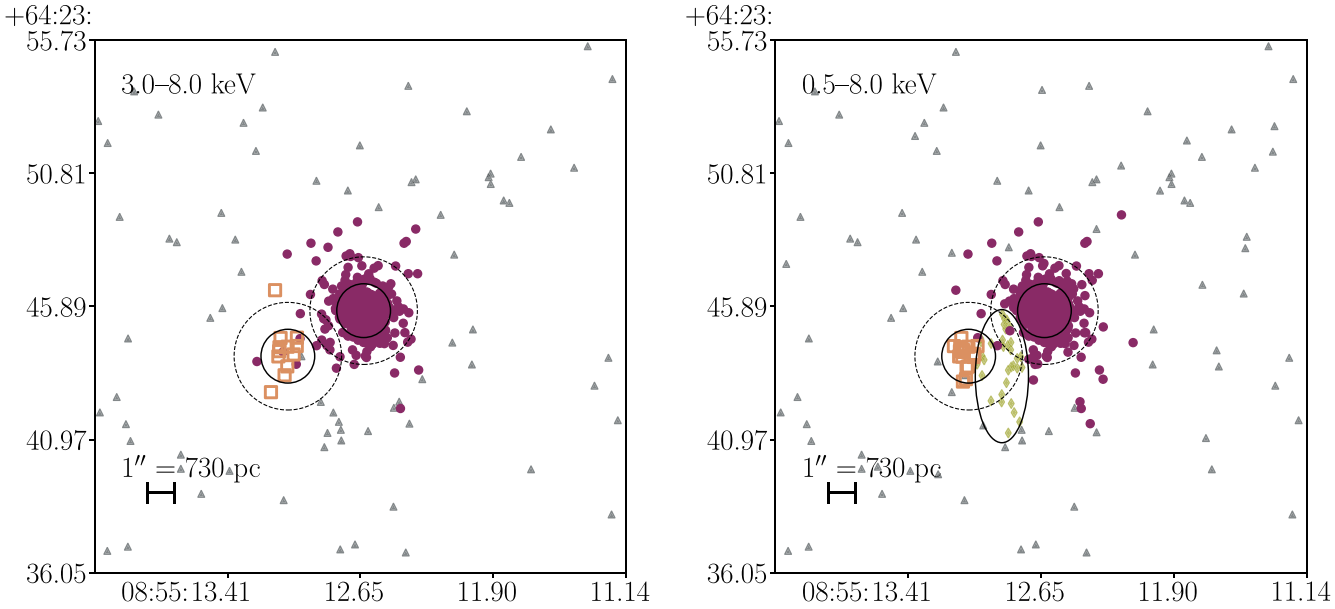

Figure 7. The unbinned 3–8 keV (left) and 0.5–8 keV (right) data sets for MCG+11-11-032, where we use `BAYMAX` to probabilistically assign each count to different model components. Here, the counts most likely associated with the primary are denoted by the red circles, the counts most likely associated with the secondary are denoted by the open-faced squares, the counts most likely associated with the background are denoted by the gray triangles, and, in the right panel, the counts most likely associated with a high-count diffuse emission component are shown by the green diamonds. With the solid (dashed) black lines, we plot $1''$ ($2''$) radius circles centered on the best-fit location for the primary and secondary point sources. When analyzing the 3–8 keV data set with `BAYMAX`, which excludes photons associated with an extended and soft component, we find a logBF $= 9.38 \pm 1.95$, in favor of the dual-point-source model. The position of the secondary is consistent with our findings when analyzing the full data set (see Section 3.1 for more details). When analyzing the full 0.5–8 keV data set with an additional model component that accounts for a high-count diffuse emission region (sitting within the black ellipse shown in the right panel), we find a Bayes factors of logBF $= 28.6 \pm 2.2$, in favor of the dual-point-source model. Even with an additional high-count component included in our models, we find strong evidence for the presence of a point source.

ORCID iDs

Adi Foord https://orcid.org/0000-0002-1616-1701
Francesca Civano https://orcid.org/0000-0002-2115-1137
Julia M. Comerford https://orcid.org/0000-0001-8627-4907
Martin Elvis https://orcid.org/0000-0001-5060-1398
Giuseppina Fabbiano https://orcid.org/0000-0002-3554-3318
Tingting Liu https://orcid.org/0000-0001-5766-4287
Elisabeta Lusso https://orcid.org/0000-0003-0083-1157
Stefano Marchesi https://orcid.org/0000-0001-5544-0749
Mar Mezcua https://orcid.org/0000-0003-4440-259X
Francisco Muller-Sanchez https://orcid.org/0000-0002-2713-0628
Rebecca Nevin https://orcid.org/0000-0003-1056-8401
Kristina Nyland https://orcid.org/0000-0003-1991-370X

References

Akaike, H. 1974, ITAC, 19, 716
Anastasopoulou, K., Zezas, A., Steiner, J. F., & Reig, P. 2022, MNRAS, 513, 1400
Arnaud, K. A. 1996, in ASP Conf. Ser. 101, Astronomical Data Analysis Software and Systems V, ed. G. H. Jacoby & J. Barnes (San Francisco, CA: ASP), 17
Bachetti, M., Harrison, F. A., Walton, D. J., et al. 2014, Natur, 514, 202
Barrows, R. S., Mezcua, M., & Comerford, J. M. 2019, ApJ, 882, 181
Barrows, R. S., Mezcua, M., Comerford, J. M., & Stern, D. 2024, ApJ, 964, 187
Basko, M. M., & Sunyaev, R. A. 1976, MNRAS, 175, 395
Bauer, F. E., Alexander, D. M., Brandt, W. N., et al. 2004, AJ, 128, 2048
Becker, R. H., White, R. L., & Helfand, D. J. 1995, ApJ, 450, 559
Begelman, M. C. 2002, ApJL, 568, L97
Bianchi, S., Chiaberge, M., Evans, D. A., et al. 2010, MNRAS, 405, 553
Bianchi, S., Guainazzi, M., & Chiaberge, M. 2006, A&A, 448, 499
Brightman, M., Nandra, K., Salvato, M., et al. 2014, MNRAS, 443, 1999
Brightman, M., & Ueda, Y. 2012, MNRAS, 423, 702
Buchner, J., Georgakakis, A., Nandra, K., et al. 2014, A&A, 564, A125
Calistro Rivera, G., Williams, W. L., Hardcastle, M. J., et al. 2017, MNRAS, 469, 3468
Canuto, V., & Chou, C. K. 1971, Ap&SS, 10, 246
Cash, W. 1979, ApJ, 228, 939
Colbert, E. J. M., & Mushotzky, R. F. 1999, ApJ, 519, 89
Colpi, M., & Dotti, M. 2011, ASL, 4, 181
Comerford, J. M., Gerke, B. F., Stern, D., et al. 2012, ApJ, 753, 42
Corral, A., Della Ceca, R., Caccianiga, A., et al. 2011, A&A, 530, A42
Cseh, D., Webb, N. A., Godet, O., et al. 2015, MNRAS, 446, 3268
Davis, J. E., Bautz, M. W., Dewey, D., et al. 2012, Proc. SPIE, 8443, 84431A
Davis, S. W., Narayan, R., Zhu, Y., et al. 2011, ApJ, 734, 111
Derdzinski, A., D'Orazio, D., Duffell, P., Haiman, Z., & MacFadyen, A. 2021, MNRAS, 501, 3540
D'Orazio, D. J., & Duffell, P. C. 2021, ApJL, 914, L21
D'Orazio, D. J., Haiman, Z., Duffell, P., MacFadyen, A., & Farris, B. 2016, MNRAS, 459, 2379
D'Orazio, D. J., Haiman, Z., & MacFadyen, A. 2013, MNRAS, 436, 2997
Duffell, P. C., D'Orazio, D., Derdzinski, A., et al. 2020, ApJ, 901, 25
Eksi, K. Y., Andac, I. C., Cikintoglu, S., et al. 2015, MNRAS, 448, L40
Farrell, S. A., Servillat, M., Pforr, J., et al. 2012, ApJL, 747, L13
Farrell, S. A., Webb, N. A., Barret, D., Godet, O., & Rodrigues, J. M. 2009, Natur, 460, 73
Farris, B. D., Duffell, P., MacFadyen, A. I., & Haiman, Z. 2014, ApJ, 783, 134
Farris, B. D., Duffell, P., MacFadyen, A. I., & Haiman, Z. 2015, MNRAS, 446, L36
Foord, A., Gültekin, K., Nevin, R., et al. 2020, ApJ, 892, 29
Foord, A., Gültekin, K., Reynolds, M. T., et al. 2019, ApJ, 877, 17
Foord, A., Gültekin, K., Runnoe, J. C., & Koss, M. J. 2021, ApJ, 907, 71
Fotopoulou, S., Buchner, J., Georgantopoulos, I., et al. 2016, A&A, 587, A142
Fruscione, A., McDowell, J. C., Allen, G. E., et al. 2006, Proc. SPIE, 6270, 62701V
Gao, Y., Wang, Q. D., Appleton, P. N., & Lucas, R. A. 2003, ApJL, 596, L171
Giroletti, M., & Panessa, F. 2009, ApJL, 706, L260
Godet, O., Plazolles, B., Kawaguchi, T., et al. 2012, ApJ, 752, 34
Gold, R., Paschalidis, V., Ruiz, M., et al. 2014, PhRvD, 90, 104030
Gong, H., Liu, J., & Maccarone, T. 2016, ApJS, 222, 12
Greene, J. E., Strader, J., & Ho, L. C. 2020, ARA&A, 58, 257
Gültekin, K., Cackett, E. M., King, A. L., Miller, J. M., & Pinkney, J. 2014, ApJL, 788, L22
Gültekin, K., King, A. L., Cackett, E. M., et al. 2019, ApJ, 871, 80
Hasinger, G. 2008, A&A, 490, 905
Hopkins, P. F., Hernquist, L., Cox, T. J., & Kereš, D. 2008, ApJS, 175, 356
Kaaret, P., & Feng, H. 2007, ApJ, 669, 106
Kaaret, P., Feng, H., & Roberts, T. P. 2017, ARA&A, 55, 303
King, A., Lasota, J.-P., & Middleton, M. 2023, NewAR, 96, 101672
King, A. R., Davies, M. B., Ward, M. J., Fabbiano, G., & Elvis, M. 2001, ApJL, 552, L109
Lamperti, I., Koss, M., Trakhtenbrot, B., et al. 2017, MNRAS, 467, 540
Lasota, J. P., Alexander, T., Dubus, G., et al. 2011, ApJ, 735, 89
Lehmer, B. D., Eufrasio, R. T., Tzanavaris, P., et al. 2019, ApJS, 243, 3
Levenson, N. A., Heckman, T. M., Krolik, J. H., Weaver, K. A., & Życki, P. T. 2006, ApJ, 648, 111
Liu, T., Koss, M., Blecha, L., et al. 2020, ApJ, 896, 122
Lusso, E., Comastri, A., Simmons, B. D., et al. 2012, MNRAS, 425, 623
Maccarone, T. J. 2003, A&A, 409, 697
Maccarone, T. J. 2005, MNRAS, 360, L68
MacFadyen, A. I., & Milosavljević, M. 2008, ApJ, 672, 83
Magdziarz, P., & Zdziarski, A. A. 1995, MNRAS, 273, 837
Matsumoto, H., Tsuru, T. G., Watari, K., Mineshige, S., & Matsushita, S. 2003, in ASP Conf. Ser. 289, The Proceedings of the IAU 8th Asian-Pacific Regional Meeting, 1, ed. S. Ikeuchi, J. Hearnshaw, & T. Hanawa (San Francisco, CA: ASP), 291
Merloni, A., Heinz, S., & di Matteo, T. 2003, MNRAS, 345, 1057
Mezcua, M. 2017, IJMPD, 26, 1730021
Mezcua, M., Farrell, S. A., Gladstone, J. C., & Lobanov, A. P. 2013, MNRAS, 436, 1546
Mezcua, M., Roberts, T. P., Lobanov, A. P., & Sutton, A. D. 2015, MNRAS, 448, 1893
Middleton, M. J., Heil, L., Pintore, F., Walton, D. J., & Roberts, T. P. 2015, MNRAS, 447, 3243
Miller, J. M., Fabian, A. C., & Miller, M. C. 2004, ApJL, 614, L117
Mineo, S., Gilfanov, M., & Sunyaev, R. 2012, MNRAS, 419, 2095
Moody, M. S. L., Shi, J.-M., & Stone, J. M. 2019, ApJ, 875, 66
Musaeva, A., Koribalski, B. S., Farrell, S. A., et al. 2015, MNRAS, 447, 1951
Mushtukov, A. A., Suleimanov, V. F., Tsygankov, S. S., & Poutanen, J. 2015, MNRAS, 454, 2539
Nevin, R., Comerford, J., Müller-Sánchez, F., Barrows, R., & Cooper, M. 2016, ApJ, 832, 67
Panessa, F., Barcons, X., Bassani, L., et al. 2007, A&A, 467, 519
Pasham, D. R., & Strohmayer, T. E. 2013, ApJL, 774, L16
Perley, R. A., Chandler, C. J., Butler, B. J., & Wrobel, J. M. 2011, ApJL, 739, L1
Pizzolato, F., Wolter, A., & Trinchieri, G. 2010, MNRAS, 406, 1116
Poutanen, J., Lipunova, G., Fabrika, S., Butkevich, A. G., & Abolmasov, P. 2007, MNRAS, 377, 1187
Predehl, P., & Schmitt, J. H. M. M. 1995, A&A, 293, 889
Reynolds, C. S., Kara, E. A., Mushotzky, R. F., et al. 2023, Proc. SPIE, 12678, 126781E
Salim, S., Boquien, M., & Lee, J. C. 2018, ApJ, 859, 11
Salvatier, J., Wiecki, T. V., & Fonnesbeck, C. 2016, PeerJ Comput. Sci., 2, e55
Sandoval, B., Foord, A., Allen, S. W., et al. 2024, ApJ, 974, 121
Servillat, M., Farrell, S. A., Lin, D., et al. 2011, ApJ, 743, 6
Severgnini, P., Cicone, C., Della Ceca, R., et al. 2018, MNRAS, 479, 3804
Shimwell, T. W., Hardcastle, M. J., Tasse, C., et al. 2022, A&A, 659, A1
Soria, R., Hau, G. K. T., Graham, A. W., et al. 2010, MNRAS, 405, 870
Soria, R., Hau, G. K. T., & Pakull, M. W. 2013, ApJL, 768, L22
Straub, O., Godet, O., Webb, N., Servillat, M., & Barret, D. 2014, A&A, 569, A116
Strohmayer, T. E., & Mushotzky, R. F. 2009, ApJ, 703, 1386
Sutton, A. D., Roberts, T. P., Gladstone, J. C., & Walton, D. J. 2015, MNRAS, 450, 787
Sutton, A. D., Roberts, T. P., Walton, D. J., Gladstone, J. C., & Scott, A. E. 2012, MNRAS, 423, 1154
Tang, Y., Haiman, Z., & MacFadyen, A. 2018, MNRAS, 476, 2249
Taniguchi, Y., Shioya, Y., Tsuru, T. G., & Ikeuchi, S. 2000, PASJ, 52, 533
Terashima, Y., & Wilson, A. S. 2003, ApJ, 583, 145
Tiede, C., Zrake, J., MacFadyen, A., & Haiman, Z. 2020, ApJ, 900, 43
Tozzi, P., Gilli, R., Mainieri, V., et al. 2006, A&A, 451, 457
Travascio, A., Fabbiano, G., Paggi, A., et al. 2021, ApJ, 921, 129
Tsygankov, S. S., Mushtukov, A. A., Suleimanov, V. F., & Poutanen, J. 2016, MNRAS, 457, 1101
Volonteri, M., Lodato, G., & Natarajan, P. 2008, MNRAS, 383, 1079
Wang, J.-M., Chen, Y.-M., Hu, C., et al. 2009, ApJL, 705, L76
Webb, N. A., Barret, D., Godet, O., et al. 2010, ApJL, 712, L107
Webb, N. A., Guérou, A., Ciambur, B., et al. 2017, A&A, 602, A103
Whitley, K., Kuznetsova, A., Gültekin, K., & Ruszkowski, M. 2024, MNRAS, 527, 6569
Wiersema, K., Farrell, S. A., Webb, N. A., et al. 2010, ApJL, 721, L102
Wolter, A., Trinchieri, G., & Colpi, M. 2006, MNRAS, 373, 1627
Yan, C.-S., Lu, Y., Dai, X., & Yu, Q. 2015, ApJ, 809, 117
Zolotukhin, I., Webb, N. A., Godet, O., Bachetti, M., & Barret, D. 2016, ApJ, 817, 88